Fuel 319 (2022) 123827

Contents lists available at ScienceDirect

Fuel

journal homepage: www.elsevier.com/locate/fuel

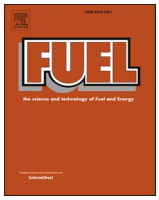

Full Length Article

Tailoring the selectivity of Cu-based catalysts in the furfural hydrogenation reaction: Influence of the morphology of the silica support

C.P. Jiménez-Gómez [a], J.A. Cecilia [a], A.C. Alba-Rubio [b,1], A. Cassidy [b], R. Moreno-Tost [a], C. García-Sancho [a,*], P. Maireles-Torres [a]

[a] Universidad de Málaga, Departamento de Química Inorgánica, Cristalografía y Mineralogía (Unidad Asociada al ICP-CSIC), Facultad de Ciencias, Campus de Teatinos, 29071 Málaga, Spain

[b] Department of Chemical Engineering, The University of Toledo, Toledo, OH 43606, USA

ARTICLE INFO

Keywords:
2-Methylfuran
Furfural
Hydrogenation
Mesoporous silica
Cu-based catalysts
Strong Electrostatic Adsorption

ABSTRACT

Cu nanoparticles were incorporated on different porous silica supports (commercial silica, SBA-15 synthesized both at room temperature and under hydrothermal conditions, and mesocellular foam) by the strong electrostatic adsorption method and tested in the gas-phase furfural hydrogenation for the production of furfuryl alcohol and 2-methylfuran, being the latter a promising biofuel. The incorporated copper species provided metal particle sizes lower than 5 nm in all cases. However, different catalytic behaviors, both in terms of conversion and selectivity, were detected due to the morphology and textural properties of each support. Cu over commercial silica was more prone to suffer from deactivation, and it provided higher furfuryl alcohol yields, probably due to its higher acidity and lower metallic surface area. On the other hand, the agglomeration of Cu nanoparticles together with larger pore sizes complicated the access of furfural to the active sites using the hydrothermal SBA-15 support, thus decreasing the activity. In contrast, the addition of fluoride in the synthesis of mesoporous silica, which shortened the length of the silica channels (mesocellular foam), facilitated the furfural access and provided both higher metallic surface area and lower acidity. This fact led to a more gradual deactivation, still attaining high values of furfural conversion and 2-methylfuran yield (95 and 76%, respectively) after 5 h at 190 °C. However, Cu over mesocellular foam changed its selectivity pattern along 48 h and after regeneration, increasing the furfuryl alcohol selectivity due to the decreased number of available active sites.

1. Introduction

The depletion of fossil reserves in the last century and the high volume of emissions generated have led to search and develop more environmentally friendly alternative energy sources. In this sense, biomass is an attractive alternative since it is the only source from which both energy and chemicals can be obtained, making it the only one with enough potential to replace fossil fuels completely [1]. Even when biomass is widely distributed on Earth, the type of biomass must be carefully selected since, in some cases, the biomass used to obtain energy and chemicals can compete with the food supply [2]. This fact could cause an increase in prices due to the reduction of farmland for food and speculation leading to social imbalances. Among the wide variety of biomass sources, lignocellulosic biomass has emerged as a relevant sustainable source since it does not interfere with the food chain, it is very abundant, and it aims to valorize agricultural residues to produce high value-added chemicals [1,3]. Lignocellulose is generally composed of cellulose, hemicellulose, and lignin, as well as some minor non-structural components, such as proteins, chlorophylls, ash, waxes, tannins (in the case of wood), and pectin (in most fibers) [4]. Focusing on hemicellulose, which displays a disordered and branched structure (with short lateral chains) and low molecular weight, this can be relatively easy to hydrolyze in their respective monomers (pentoses), mainly xylose and arabinose [5].

Then, these C5 monomers can be dehydrated through acid catalysis to give rise to furfural (FUR) as the main product [6,7]. This molecule is considered one of the most interesting of the sugar platform in biorefineries, with an annual world production of about 430,000 tons [8,9]. FUR possesses numerous industrial applications, such as fungicide, nematicide, specialized adhesive, flavoring compound, and for the

* Corresponding author.
E-mail address: cristinags@uma.es (C. García-Sancho).
[1] Present address: Departament of Chemical and Biomolecular Engineering, Clemson University, Clemson, SC 29634, USA.

https://doi.org/10.1016/j.fuel.2022.123827
Received 26 January 2022; Accepted 7 March 2022
Available online 16 March 2022

recovery of refinery lubricants, although FUR is mainly employed as a precursor for a wide variety of high value-added chemicals that can be obtained through hydrogenation, oxidation, dehydration, condensation or opening-ring reactions [10–12]. Among them, the hydrogenation of furfural is the reaction that possesses the greatest commercial interest. Thus, it has been reported that about 62% of FUR is employed to synthesize furfuryl alcohol (FOL) by hydrogenation [12]. Commercially, this chemical transformation has been carried out by using copper chromite as the catalyst for more than 80 years [13–16]. However, the stringent environmental regulations related to Cr species, together with the high susceptibility of these catalysts to undergo deactivation [17], have led researchers to develop highly active and selective Cr-free catalysts [12]. In this sense, several authors have demonstrated that non-noble metals, such as Cu-, Ni-, and bimetallic-based catalysts [11,12,18], as well as noble metals (Ru, Pt, Pd, Au) [19–25] can attain a suitable catalytic performance. As FUR is highly reactive, both the hydrogenating character and the acid/base properties of catalysts need to be modulated. For example, even when Ni-based catalysts are highly active, they are not very selective in many cases because their active centers interact with both the carbonyl group and the aromatic furan ring [26–30]. However, Cu-based catalysts have displayed a lower hydrogenating capacity than the Ni ones, which implies that the active sites only interact with the carbonyl group [26,31–33], in such a way that the formation of furfuryl alcohol and 2-methylfuran (MF) is favored [26,31,34–38]. Fortunately, both compounds are considered valuable FUR derivatives, since FOL is employed in the resin manufacture for the foundry industry and as a starting compound for the synthesis of agrochemicals and bioproducts [12], while MF has potential to be used as additive for biofuels and for the synthesis of heterocycles [12]. On the other hand, it has been reported in the literature that the amount and the strength of acid sites also play an important role in determining the catalytic activity and selectivity. The presence of a high concentration of acid sites favors the FUR polymerization and causes the formation of carbonaceous deposits, leading to the partial blockage of active sites for FUR hydrogenation [17,37]. Generally, the use of Cu-based catalysts in the gas-phase hydrogenation of furfural results in FOL as the main product, while the formation of MF is quite low [33]. However, several papers have reported that the presence of weak acidity and small metal Cu nanoparticles bring about the hydrogenolysis of FOL to MF [35,37].

As non-noble metal catalysts are prone to deactivation, most catalysts are prepared with a very high metal loading. One of the greatest challenges for the scientific community is to design catalysts in which textural properties, the proportion of acid and basic sites, and the nanoparticle size of the active phase can be easily modulated. For example, Jiao et al. [39] dispersed several metals, Cu among them, on different supports by using the strong electrostatic adsorption (SEA) method and compared them with others prepared by the conventional incipient wetness impregnation approach. They showed that the SEA method provided better metal dispersion, easier reducibility, and smaller particle size. Recently, Wong et al. [40] attained much lower metal particle sizes on silica supports (0.9–1.4 nm), in comparison with metal particles obtained by conventional impregnation (4.2–15 nm), after studying different supported metal catalysts, including Cu-based ones. Regarding the textural properties, the synthesis of porous silica-based solids with ordered structure has grown exponentially [41]. SBA-15 has been the most studied mesostructure in the last 20 years for its applications in the fields of adsorption and catalysis [42]. This mesostructured silica displays a hexagonal ordering formed by parallel cylindrical channels with a diameter between 4 and 9 nm [43], although the main advantage is ascribed to the ease of preparation, good thermal and mechanical resistance, and the tunability of the pore size. However, one of the main disadvantages of mesoporous materials is that, in some cases, active metal nanoparticles are greater than the pore diameter of the support, so these nanoparticles remain on their outer surface, leaving a significant fraction of their specific surface area without active phase. On the other hand, the long length of the cylindrical mesochannels facilitates the deactivation, and, in many cases, these pores are too narrow to allow the access of reagents to the active sites. Additionally, these narrow pores can be easily blocked by the strong interaction of the reactants or products with the active centers, or by the formation of coke [44]. To overcome those challenges, the pore diameter of the mesochannels can be enlarged by the incorporation of aromatics [45,46], alkanes [47,48], or amines [49] in the synthesis gel, although this strategy often promotes the loss of ordering in the porous silica [46]. On the other hand, incorporating fluoride species in the synthetic step limits the growth of the mesochannel length, obtaining other structures with poorer ordering denoted as mesocellular foams [45,46,50].

Considering these premises, this work aimed to study the effect of the textural properties of several porous silicas on the dispersion of Cu nanoparticles by using strong electrostatic adsorption (SEA) method. Thus, different synthetic strategies were employed to prepare mesoporous silica with different textural properties, and these were compared to commercial fumed silica. Although this study is focused on establishing a correlation between the textural properties and the catalytic behavior of Cu catalysts supported on mesoporous silicas, the effect of the Cu loading on the catalytic activity was also evaluated by supporting highly dispersed Cu nanoparticles on a commercial fumed silica support using the SEA method. The study of these catalysts in the gas-phase hydrogenation of furfural allowed us to establish a correlation between the number of available metal sites and the catalytic activity. Additionally, an analysis of the deactivation processes is performed, and a strategy for the regeneration of the catalysts is put forward.

2. Materials and methods

2.1. Reagents

The chemicals used for the synthesis of the porous silica were P123 Pluronic ($PEO_{20}PPO_{70}PEO_{20}$, average $M_n \sim 5800$, Sigma-Aldrich) as a template, tetraethylorthosilicate (TEOS) (Aldrich, 98%) as the silicon source, and hydrochloric acid (HCl) (VWR, 37%). For the modification of the textural properties of porous silica, ammonium fluoride (NH_4F) (Aldrich, 99%) was employed. Commercial CAB-O-SIL® EH-5 fumed silica was also used. Before using it as a support, it was washed to remove any potential metal impurities with a 0.1 M HNO_3 aqueous solution for 1 h at room temperature; then, the solution was filtered and washed with deionized water until neutral pH and dried at 60 °C for 24 h. In all cases, Cu was incorporated by using $[Cu(NH_3)_4]SO_4{\cdot}H_2O$ (Sigma-Aldrich, 98%) as the metal precursor. Furfural (FUR) (Sigma-Aldrich, 99%) and cyclopentyl methyl ether (CPME) (Sigma-Aldrich, 99.9%) were employed in the hydrogenation reactions. Likewise, the gases utilized were H_2 (Air Liquide 99.999%), He (Air Liquide 99.99%), H_2/Ar (10% vol. H_2, Air Liquide 99.99%), N_2 (Air Liquide 99.9999%), and N_2O/He (35% vol. N_2O, Air Liquide 99.99%).

2.2. Synthesis of the porous silicas

The synthesis of the SBA-15 was carried out by adjusting the temperature of the hydrothermal treatment, following the method previously described by Fulvio et al. [51]. Briefly, Pluronic P123 was dissolved in a 1.7 M HCl aqueous solution under stirring at 40 °C. Once P123 was dissolved, the silicon source (TEOS) was added dropwise to the mother solution to obtain a gel with a molar ratio of 1 P123: 55 SiO_2: 350 HCl: 11,100 H_2O. This gel was stirred at 40 °C for 24 h and, on the one hand, it was aged at room temperature for 48 h in order to obtain a porous SBA-15 silica with narrower pore diameter (SBA-LT) and, on the other hand, it was transferred to a Teflon-lined autoclave, where it was aged under hydrothermal conditions at 120 °C for 48 h to get a SBA-15 with a wider pore diameter (SBA-HT).

In another synthesis, and in order to modify the textural properties of the SBA-15, NH_4F was incorporated into the synthesis step. The

synthesis of this modified porous silica was carried out following the synthesis described by Santos et al. [52] in such a way that firstly, both the template (P123) and NH_4F were dissolved in a 1.7 M HCl aqueous solution under stirring at 40 °C. After the total dissolution of the template, the silicon source, TEOS, was also incorporated. The final gel had a molar ratio of 1 P123: 1.8 NH_4F: 350 HCl: 55 SiO_2: 11,100 H_2O. Finally, the obtained gel was stirred at 40 °C for 24 h, and then it was aged for 48 h at room temperature. Santos et al. [52] reported that the obtained material displayed a structure with shorter channels, being denoted as mesocellular foam (MFC-LT).

In all cases, the obtained gel was washed with distilled water, filtered, and dried overnight at 80 °C. Finally, all the solids were calcined at 550 °C for 6 h (heating rate of 1 °C min^{-1}).

The physicochemical properties of the obtained porous silicas were compared with those of a fumed silica with submicron particle size provided by Cabot Corporation.

Once porous silicas were synthesized and characterized, Cu was incorporated through the strong electrostatic method (SEA). This consists of preparing a dispersion of the support in water and selecting a pH above its point of zero charge (PZC) in order to have a negatively charged surface, thus promoting the interaction with $Cu(NH_3)_4^{2+}$ species, which results in highly dispersed Cu nanoparticles on silica [39]. For this, 2 g of porous silica was added to 1 L of deionized water under stirring. In the next step, an aqueous solution of $[Cu(NH_3)_4]SO_4{\cdot}H_2O$ was added to obtain a final copper loading of 10 wt%. Then, the pH of the solution was adjusted with diluted NH_3 and H_2SO_4 solutions to pH = 9. Later, the solution was stirred for 20 h at room temperature, and, after that, it was filtered and washed with deionized water, thus obtaining the pertinent catalytic precursors. However, in no case coloration was observed in the washing liquid, so all the $Cu(NH_3)_4^{2+}$ species were incorporated to the supports.

The catalyst precursor was thermally treated to decompose the salt and reduce the metal phase in the same process. To do so, the catalytic precursors were heated with a heating rate of 5 °C min^{-1} from room temperature up to 300 °C under a He flow (60 mL min^{-1}). Then, the gas carrier was changed to H_2 (60 mL min^{-1}) and the temperature was increased up to 400 °C (5 °C min^{-1}), which was maintained for 3 h in order to reduce copper species. Later, the gas was switched back to He again, and the sample was maintained at 400 °C for 1 h before cooling down to room temperature under He flow. Finally, the catalysts were passivated using 0.5 vol% O_2/N_2 for 30 min at room temperature.

The samples were labeled as XCu-Y, where X indicates the theoretical metal Cu loading, expressed as wt.%, and Y the support employed. Thus, the following catalysts were synthesized: XCu-SBA-LT for the Cu-based catalyst supported on SBA-15 aged at room temperature, XCu-SBA-HT for the Cu-based catalyst supported on SBA-15 aged at 120 °C, XCu-MCF-LT for the Cu-based catalyst supported on mesocellular foam, and XCu-SiO_2 for the Cu-based catalysts supported on a commercial fumed silica. First, the effect of adding different Cu loadings (2.5–20 wt %) was evaluated by using the commercial silica as the support (XCu-SiO_2). Then, an intermediate loading of 10 wt% Cu was chosen to evaluate the influence of each support on the furfural hydrogenation (SBA-LT, SBA-HT, and MCF-LT).

2.3. Characterization of catalysts

Small-angle X-ray scattering (SAXS) measurements were collected on a D8 DISCOVER-Bruker instrument at 40 mA and 40 kV. Powder patterns were recorded in capillary transmission configuration by using a LYNXeye detector and a Göbel mirror ($CuK\alpha_1$ radiation). The powder patterns were performed between 0.2 and 10°, with a total measuring time of 120 min.

X-ray diffraction (XRD) patterns of the Cu-based catalysts were obtained by using the Bragg–Brentano reflection configuration in a PAN-analytical X'Pert Pro automated diffractometer equipped with a Ge (1 1 1) primary monochromator (strictly monochromatic $CuK\alpha_1$) and an X'Celerator detector with a step size of 0.0178 (2θ) between 2θ = 10 and 70°, with an equivalent counting time of 712 s per step. The crystalline particle size (D) was evaluated by using the Williamson–Hall equation, $B\cos\theta = (K\lambda/D) + (2\varepsilon \sin\theta)$, where B is the full width at half-maximum (FWHM) of the XRD peak, θ is the Bragg angle, K is the Scherrer constant, λ is the X-ray wavelength, and ε is the lattice strain [53].

A FEI Talos F200X equipment was utilized in order to study the catalyst morphology by transmission electron microscopy (TEM). This equipment combines high-resolution STEM and TEM imaging with energy-dispersive X-ray spectroscopy (EDS) signal detection, and 3D chemical characterization with compositional mapping. Samples were suspended in isopropyl alcohol and dropped onto a perforated carbon film grid.

Textural properties were obtained from the N_2 adsorption–desorption isotherms at −196 °C, as determined by an automatic Micromeritics ASAP 2420 system. Before the adsorption analysis, samples were outgassed overnight at 200 °C and 10^{-4} mbar. Surface areas were determined using the BET equation considering a N_2 cross-section of 16.2 $Å^2$ [54], while the microporosity was determined by the t-plot method [55]. The total pore volume was evaluated from the adsorption isotherm at $P/P_0 = 0.95$, and the average pore size was determined by applying the Barrett–Joyner–Halenda (BJH) method to the desorption branch [56]. On the other hand, a density functional theory (DFT) method was employed to determine the pore size distribution [57].

The number of acid sites was determined by temperature-programmed desorption of ammonia (NH_3-TPD). For each analysis, 0.08 g of catalyst was placed in a U-shaped quartz reactor and treated with H_2 (60 mL min^{-1}) at 300 °C with a heating rate of 5 °C min^{-1} to remove the passivation layer. Then, the sample was cooled in He (40 mL min^{-1}) until 100 °C, and once the temperature was reached, the sample was saturated with ammonia for 5 min, and then, a He flow was employed to remove the physisorbed NH_3. Ammonia desorption was performed by heating the sample from 100 to 300 °C, with a rate of 5 °C min^{-1}, while registering the signal using a thermal conductivity detector (TCD).

In order to know the reducibility of the catalysts, hydrogen temperature-programmed reduction (H_2-TPR) experiments were conducted. In each test, 0.08 g of the catalyst precursor was employed, being firstly treated under He (60 mL min^{-1}) at 350 °C (heating rate of 5 °C min^{-1}) for 1 h to decompose the precursor salt. After that, the sample was cooled to room temperature and the H_2 consumption was monitored between 50 and 800 °C with a heating rate of 10 °C min^{-1} by using a 10 vol% H_2/Ar flow (48 mL min^{-1}). The consumed H_2 was quantified by using an on-line TCD in such a way that the water formed in the reduction process was trapped through a cold finger immersed into a liquid N_2/isopropanol slurry (-80 °C).

The exposed Cu surface and the dispersion of Cu nanoparticles were determined by N_2O titration. This methodology is based on the superficial oxidation of Cu^0 under a N_2O flow, described in previous research [36,52], according to the reaction:

$$2Cu^0 + N_2O \rightarrow Cu_2O + N_2$$

Before the analysis, the catalytic precursor was treated under a He flow (60 mL min^{-1}) up to 350 °C (5 °C min^{-1}) for 1 h, followed by a reduction step at 300 °C for 1 h, with a heating rate of 5 °C min^{-1}, under a 10 vol% H_2/Ar flow (48 mL min^{-1}). Later, the reduced catalyst was cooled to 60 °C under a He flow. Then, the mild oxidation of Cu^0 to Cu^+ was performed by flowing N_2O (5 vol% N_2O/He) at 60 °C for 1 h. After that, the sample was cleaned under an Ar flow and cooled to room temperature. Finally, the Cu_2O reduction to Cu^0 was performed by heating the sample from room temperature to 300 °C, under a 10 vol% H_2/Ar flow (48 mL min^{-1}) with a heating rate of 5 °C min^{-1}, by using a TCD to quantify the H_2 consumption.

The metallic surface area was estimated according to the equation proposed by Pakharukova et al. [58] (Eq. (1)):

$$S_{Cu}^{N_2O}\left(m^2\ g_{Cu}^{-1}\right) = \frac{M_{H_2}\cdot SF\cdot N_A}{10^4\cdot C_M\cdot W_{Cu}} \quad (1)$$

where M_{H_2} is the number of mol of hydrogen consumed per unit mass of catalyst (μmol H_2 g_{cat}^{-1}), SF is the stoichiometric factor whose value is 2, N_A is the Avogadro number, C_M is the number of copper atoms per surface area unit ($1.46{\cdot}10^{19}$ atom m^{-2}), and W_{Cu} is the Cu content (wt %).

Considering the spherical morphology of Cu^0 nanoparticles, the average size (nm) ($d_{Cu}^{N_2O}$) was determined from Eq. (2):

$$d_{Cu}^{N_2O}\left(nm\right) = \frac{6\cdot 10^3}{S_{Cu}^{N_2O}\cdot \rho_{Cu}} \quad (2)$$

where ρ is the density of copper (8.92 g cm^{-3}).

The dispersion of the Cu^0 nanoparticles was determined by Eq. (3) [59]:

$$Dispersion(\%) = \frac{6\cdot\frac{v_{Cu}}{a_{Cu}}}{d}\cdot 100 \quad (3)$$

where v_{Cu} is the occupied volume per atom ($1.183{\cdot}10^{-29}$ m^3 $atom^{-1}$), a_{Cu} is the occupied surface per atom ($6.85{\cdot}10^{-20}$ m^2 $atom^{-1}$), and d is the average size of the Cu^0 nanoparticles.

XPS spectra were obtained in a Physical Electronics PHI 5700 spectrometer with non-monochromatic Mg Kα radiation (1253.6 eV, 300 W, 15 kV) and multichannel detector. Spectra of catalysts were recorded in the constant-pass energy mode at 29.35 eV using a diameter analysis area of 720 μm. Charge referencing was measured against adventitious carbon (C 1s) at 284.8 eV as binding energy (BE). The acquisition and data analysis was performed by using the PHI ACCESS ESCA-V6.0F software package. A Shirley-type background was subtracted from the signals. All the recorded spectra were fitted with Gaussian-Lorentzian curves to determine the binding energies of the different element core levels more accurately. As the catalysts were previously reduced, the samples were stored in sealed vials with cyclohexane as inert solvent to avoid their oxidation. Thus, the samples were prepared in a dry box under a N_2 flow and analyzed directly without previous treatment, and the solvent was evaporated before the introduction of the samples into the analysis chamber.

2.4. Catalytic studies

The gas-phase hydrogenation of FUR was carried out in a ¼" tubular quartz reactor. The pelletized catalyst (325–400 μm) was placed in the middle section between two layers of quartz wool, discarding diffusion problems through the Weiss-Prater criterion as shown in a previous publication [60]. Prior to the catalytic tests, catalysts were depassivated under a H_2 flow (60 mL min^{-1}) at 300 °C for 1 h. Then, the reduced catalysts were cooled down to the selected reaction temperature under a H_2 flow (10 mL min^{-1}). After reaching this temperature, a flow of 3.87 mL h^{-1} of a 5 vol% FUR solution in cyclopentyl methyl ether (CPME) was continuously injected using a Gilson 307SC piston pump (model 10SC). The temperature of the reaction was controlled with a thermocouple located at the same height of the catalytic bed. FUR was dissolved in CPME to avoid problems related to the use of pure furfural, such as blockage of the lines due to FUR polymerization. CPME possesses interesting physicochemical characteristics, such as that it is an environmentally friendly solvent, its low solubility in H_2O in comparison to other ethereal solvents, low boiling point (106 °C), low formation of peroxides, and relatively high stability under acid or basic conditions [38]. Liquid samples were collected and kept in sealed vials, being subsequently analyzed by using gas chromatography (Shimadzu GC-14B) with a flame ionization detector (FID) and a CP Wax 52 CB capillary column.

In a preliminary test, a Cu-SiO_2 catalyst was chosen to evaluate the stability of CPME as solvent in the absence of FUR at 190 °C after 5 h of time-on-stream (TOS). FOL and MF were the only products obtained from the hydrogenation of FUR. These products were quantified from the calibration lines obtained with commercial reagents supplied by Aldrich. The furfural conversion [%], selectivity [%] and yield [%] were calculated as follows (Eqs. (4) to (6)):

$$Conversion(\%) = \frac{mol\ of\ FUR\ converted}{mol\ of\ FUR\ fed}\cdot 100 \quad (4)$$

$$Selectivity(\%) = \frac{mol\ of\ product}{mol\ of\ FUR\ converted}\cdot 100 \quad (5)$$

$$Yield(\%) = \frac{mol\ of\ product}{mol\ of\ FUR\ fed}\cdot 100 \quad (6)$$

3. Results and discussion

3.1. Characterization of the catalysts

XRD diffraction patterns of the XCu-SiO_2 catalysts were very noisy (Fig. 1), even for the catalyst with the largest Cu loading. On 5Cu-SiO_2, diffraction peaks located at 2θ = 43.6 and 50.6°, assigned to Cu^0 crystallites, can be observed (PDF: 01-077-3038), whereas the signal located at 2θ = 36.5° was attributed to a crystalline Cu_2O phase (PDF: 01-077-0199). The analysis of crystallite sizes by the Williamson-Hall method [53] confirmed that both Cu^0 and Cu_2O must be highly dispersed as a result of the SEA method since the average crystallite size is lower than 5 nm, although the intensity of these diffraction peaks increased with the Cu loading.

On the other hand, the long-range order of porous silicas was determined by SAXS (Fig. 2). In the case of the SBA-15 supports, it can be observed a single peak attributed to the d_{100} reflection, which is shifted towards lower 2θ values when the aging temperature is increased (from 2θ = 1.03° to 0.88° for SBA-LT and SBA-HT, respectively). This shift can be due to an increase in the pore diameter, wall thickness, or both. It is also noteworthy that the intensity of SBA-LT and SBA-HT signals was similar, which could point out that the ordering of the porous structure does not depend on the synthesis temperature. Similarly, the addition of a modifying pore agent in the synthesis step to form the MFC support also caused a shift of the d_{100} reflection to a lower value (2θ = 0.36°). This fact implies a greater increase in the pore size, although the incorporation of this additive also causes a relevant decrease in the intensity of the d_{100} reflection, suggesting the formation of a structure with a lower ordering, as was previously described by other authors [48,50].

Once the ordering of the porous silicas was evaluated by SAXS, these materials were used as supports for the dispersion of Cu nanoparticles,

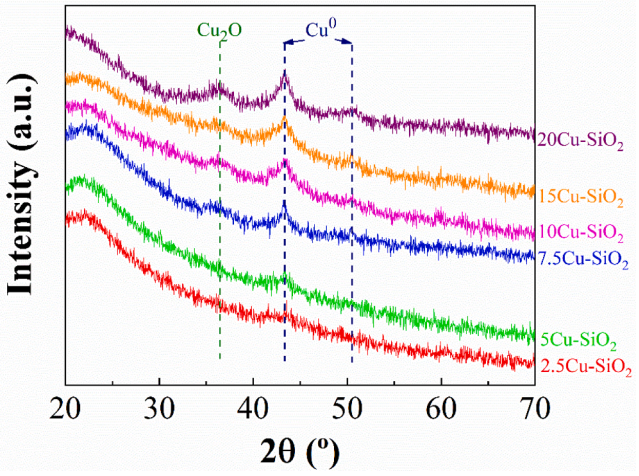

Fig. 1. X-ray diffraction of XCu-SiO_2 catalysts (X = 2.5–20 wt%).

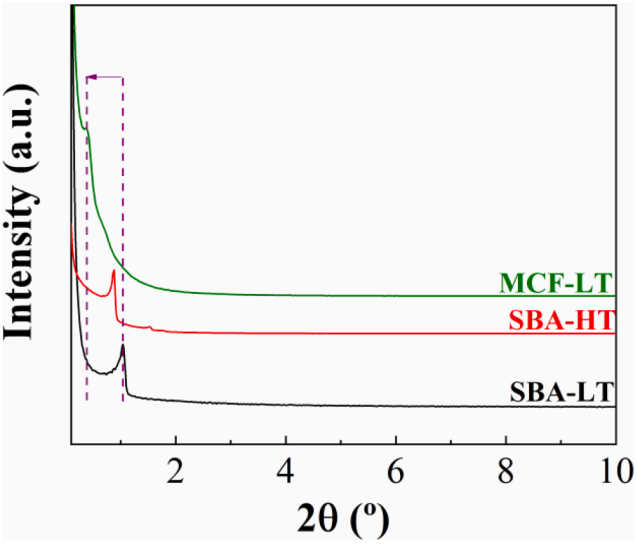

Fig. 2. Small angle X-ray scattering (SAXS) analysis of different mesoporous silicas.

which were incorporated by the SEA method. In order to compare Cu-based catalysts supported on a commercial fumed silica with those supported on mesoporous silicas, a metal loading of 10 wt% was selected. X-ray diffractograms of the reduced samples (Fig. 3) show, in all cases, a broad band at $2\theta = 23\text{-}25°$, which is assigned to the amorphous walls of porous silica. In addition, all samples exhibit intense wide and noisy diffraction peaks at $2\theta = 43.6$ and $50.6°$, which are attributed to the formation of metallic copper crystallites. Additionally, all diffractograms display another small diffraction peak located at $2\theta = 36.5°$, which is ascribed to the d_{111} reflection of Cu_2O crystallites. The presence of Cu_2O could be attributed to the partial oxidation of samples, as a result of the handling between the preparation and the XRD analysis or, most likely, to a fraction of CuO nanoparticles interacting more strongly with the support, in such a way that they are only partially reduced, forming Cu_2O crystallites. Interestingly, the modification of the support does not modify the intensity of the diffraction peaks of Cu^0 and Cu_2O. This fact implies that all the catalysts must have a similar crystallite size, which is very interesting in order to evaluate the role of the morphology of the support on the catalytic performance.

The morphology of supports and the dispersion of Cu nanoparticles

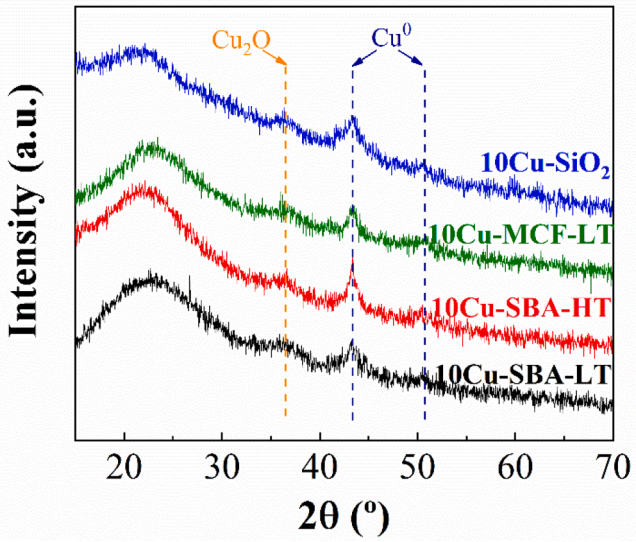

Fig. 3. X-ray diffraction of 10Cu-Y catalysts.

were determined by TEM (Fig. 4). The TEM micrograph of 10Cu-SBA-LT (Fig. 4A) evidences an ordered support with a honeycomb morphology and parallel channels. In the case of 10Cu-SBA-HT (Fig. 4B), the support maintains an ordered structure, although there is a greater separation between adjacent silica walls, in agreement with XRD data (Fig. 2). This fact would suggest the formation of a porous structure with a larger pore diameter than SBA-LT. As shown in Fig. 4C1, incorporating a structure modifying agent (MCF-LT) causes a disorder of the porous structure, as the mesochannels detected in other mesoporous silicas cannot be observed here. Regarding copper supported on commercial silica (10Cu-SiO_2) (Fig. 4D), small particles with spherical morphology can be seen. From these micrographs, it can be concluded that all the supports exhibit different morphology, which could influence their catalytic behavior. Furthermore, these micrographs also show a high dispersion of Cu nanoparticles on the different supports, with some nanoparticles small enough to enter the porous structure (Fig. 4C2), except for the 10Cu-SBA-HT catalyst where the agglomeration of small Cu crystallites can be observed on the surface of SBA-15 (Fig. 4B). This fact could be due to the hydrothermal synthesis leading to a more hydroxylated external surface than inside the pores, or the existence of regions with different points of zero charge (PZC) within the material, which could promote the strong electrostatic adsorption of Cu particles on the external surface of 10Cu-SBA-HT.

In order to determine the textural properties of catalysts, N_2 adsorption–desorption isotherms at −196 °C were obtained (Fig. S1A). According to the IUPAC classification, 10Cu-SBA-LT, 10Cu-SBA-HT, and 10Cu-MCF-LT catalysts exhibit Type IV isotherms [61], which are ascribed to mesoporous materials; however, the N_2 adsorption–desorption profiles are different due to their distinct textural properties. The isotherm of 10Cu-SiO_2 shows an increase in the N_2 adsorbed at higher relative pressure, and, unlike the other ones, it can be classified as Type II, typical of macroporous materials [61]. In this latter case, the porosity can be ascribed to interparticle voids, and the presence of the hysteresis loop suggests the presence of cavities whose size is greater than 4 nm [61]. The hysteresis loops of 10Cu-SBA-LT, 10Cu-SBA-HT, and 10Cu-MCF-LT catalysts can be considered as Type H1, found in porous materials with a narrow range of uniform mesopores [61]. However, the hysteresis loop of the 10Cu-SiO_2 catalyst resembles the Type H3, which is given by aggregates of spherical silica particles, in agreement with the results obtained by TEM (Fig. 4D).

Concerning the BET surface area (S_{BET}, Table 1) [54], 10Cu-SBA-LT, 10Cu-SBA-HT, and 10Cu-MCF-LT catalysts show very similar values (356–409 $m^2\ g^{-1}$). In contrast, 10Cu-SiO_2 possesses a much lower S_{BET} (179 m^2g^{-1}). However, the pore volume analyses evidence clearer differences than the S_{BET} values. Interestingly, while 10Cu-SBA-LT displays the lowest pore volume (V_P), the use of hydrothermal conditions (10Cu-SBA-HT) leads to the largest one. On the other hand, 10Cu-MCF-LT possesses the highest microporous surface area (t-plot, 34 m^2g^{-1}) and volume (V_{MP}, 0.0139 cm^3g^{-1}). The pore size distribution was determined by a DFT method (Fig. S1B) [57]. In all cases, the microporosity (<2 nm) was relatively low, being very similar in all of them, which is in agreement with the t-plot analysis and the micropore volume (V_{MP}). In this sense, it has been reported in the literature that the microporosity of SBA-15 is directly related to the aging temperature. Thus, several authors have affirmed that lower aging temperatures favor the interaction of the P-123 molecules with adjacent micelles, leading to structures interconnected by microchannels [46,62]. The presence of these microchannels has enormous importance in the adsorption and catalysis fields, as they might help to minimize the possible diffusion problems associated with the long mesochannels of SBA-15. However, by increasing the aging temperature, isolated P-123 micelles without connection between them are formed, which results in decreased microporosity after calcination [62]. Despite this, it has been hardly seen any differences between the microporosity of 10Cu-SBA-LT and 10Cu-SBA-HT. In this sense, it has been reported that these micropores are easily blocked when porous silicas are functionalized by grafting or

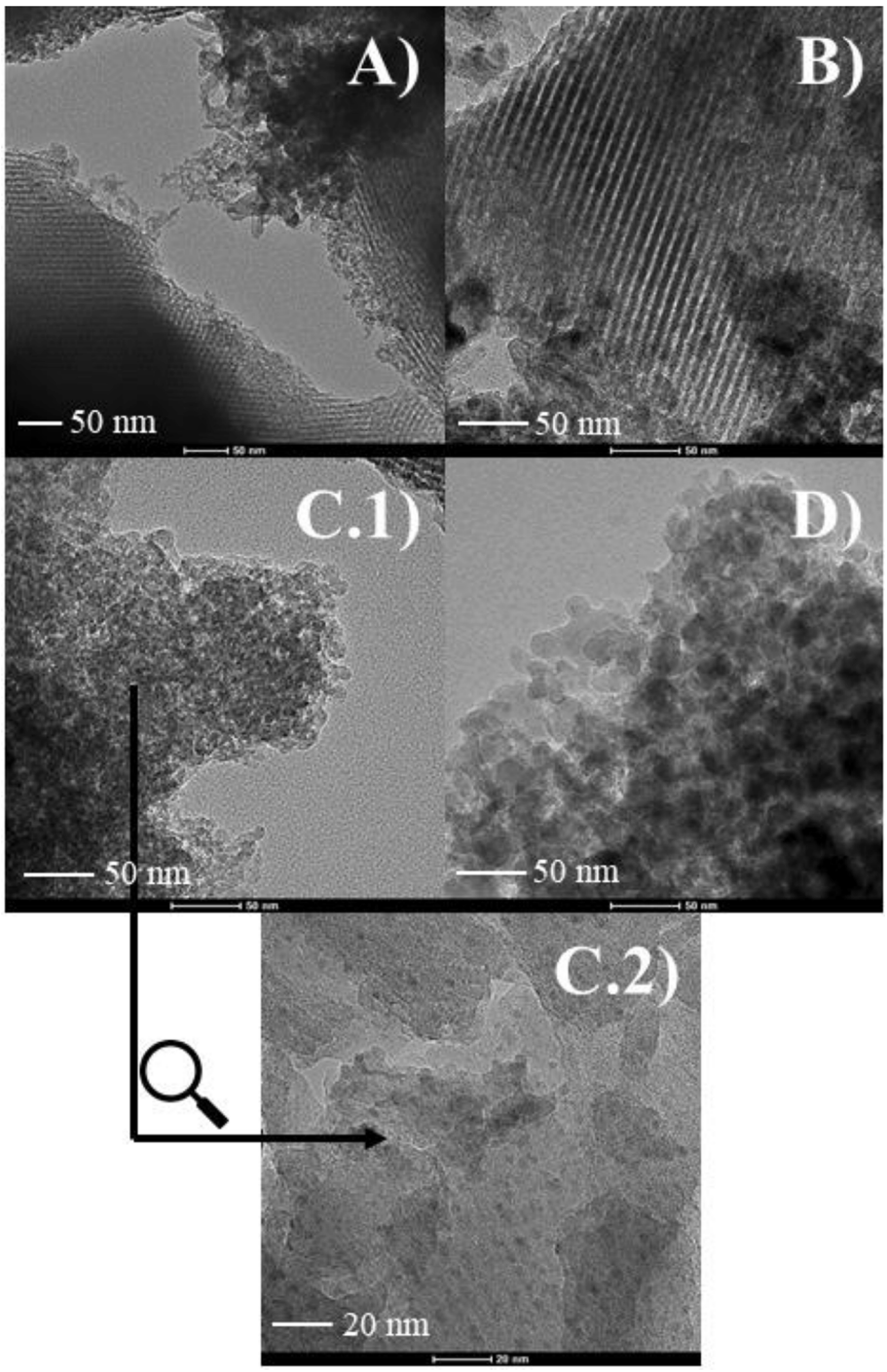

Fig. 4. TEM micrographs of 10Cu-Y catalysts: A) 10Cu-SBA-LT, B) 10Cu-SBA-HT, C) 10Cu-MCF-LT, and D) 10Cu-SiO_2.

subjected to impregnation [46]. However, regarding the mesoporosity, there are clear differences between supports (Fig. S1B). Even when 10Cu-SBA-LT, 10Cu-SBA-HT, and 10Cu-MCF-LT catalysts present a narrow distribution of pore sizes, these are centered at different pore diameters. It has been previously reported in the literature [62] that an increase in the aging temperature causes a rise of the average pore diameter (d_P); therefore, as the pore distribution for 10Cu-SBA-LT is centered at 4.3 nm and for 10Cu-SBA-HT at 8.6 nm, our results are consistent with previous studies. In the case of 10Cu-MCF-LT, the pore diameter increases compared to 10Cu-SBA-LT, which was synthesized at the same aging temperature, as a consequence of the addition of fluoride in the synthetic step that modified the growth and ordering of the porous silica, giving rise to a mesocellular structure. Finally, the 10Cu-SiO_2 catalyst does not show a homogeneous pore size distribution because its specific surface can be mainly attributed to interparticle voids between silica microspheres.

The quantification of the available Cu^0 sites was performed by N_2O titration at 60 °C (Table 2), following the methodology described in previous studies [37,38,58]. The incorporation of higher loadings of Cu species over commercial silica led to a higher metallic surface area, reaching the maximum value (25.0 $m^2_{Cu}\ g_{cat}^{-1}$) on 15Cu-SiO_2 (Table 2). However, a higher Cu loading (20Cu-SiO_2) reduces the available metallic surface area, likely due to the formation of larger Cu crystallites. Regarding the dispersion of the Cu^0 sites, a decrease is observed as

Table 1
Textural parameters and content of acid sites on 10Cu-Y catalysts.

Catalyst	S_{BET} (m^2 g^{-1})[a]	t-plot (m^2 g^{-1})[b]	V_P (cm^3 g^{-1})[c]	V_{MP} (cm^3 g^{-1})[d]	d_P (nm)[e]	Acid sites (μmol g^{-1})[f]	Acid density (μmol m^{-2})[f]
10Cu-SBA-LT	356	20	0.334	0.008	3.9	57	0.16
10Cu-SBA-HT	409	31	0.957	0.008	7.7	57	0.14
10Cu-MFC-LT	390	34	0.592	0.014	5.5	32	0.08
10Cu-SiO_2	179	23	0.548	0.007	2.1	51	0.28

[a] Specific surface area estimated by the BET equation [54].
[b] Micropore surface area estimated by the t-plot method [55].
[c] Pore volume determined by the BJH method [56].
[d] Micropore volume estimated by the t-plot method [55].
[e] Pore diameter determined by BJH method [56].
[f] Estimated by NH_3-TPD.

Table 2
Metallic properties of XCu-SiO_2 catalysts (X = 2.5–20 wt%) determined by N_2O titration.

Catalyst	Metallic surface area		Dispersion	Particle size
	m^2_{Cu} g_{Cu}^{-1}	m^2_{Cu} g_{cat}^{-1}	%	nm
2.5Cu-SiO_2	510	12.7	79	1.3
5Cu-SiO_2	394	19.7	61	1.7
7.5Cu-SiO_2	234	17.5	37	2.8
10Cu-SiO_2	182	18.2	28	3.7
15Cu-SiO_2	168	25.0	26	4.0
20Cu-SiO_2	111	22.4	18	5.8

the Cu content increases.

Regarding the influence of the support (10Cu-Y catalysts) (Table 3), 10Cu-MCF-LT displays the highest metallic surface area, 25.9 m^2_{Cu} g_{cat}^{-1}, revealing the highest Cu dispersion and the lowest particle size (2.6 nm). On the contrary, the 10Cu-SiO_2 catalyst shows the lowest metallic surface area and the largest Cu particle size for the same theoretical Cu loading. However, in all cases, the average Cu particle size, estimated by N_2O titration, is lower than 5 nm, which is in agreement with previous studies using the SEA method [39,63,64], thus corroborating that this methodology provides highly dispersed metal particles in comparison with other conventional methods, such as incipient wetness impregnation or precipitation [64].

The reducibility of the $Cu(NH_3)_4^{2+}$ species was elucidated from their H_2-TPR profiles (Fig. 5). Considering that all catalysts possess the same Cu loading (10 wt%) and a silica support, the reducibility of the Cu nanoparticles should only be attributed to their size because the interaction should be similar. In this sense, it has been reported in the literature that sometimes it is not feasible to distinguish the different reduction steps for copper species ($Cu^{2+} \rightarrow Cu^{+} \rightarrow Cu^{0}$) [37]. As shown in Fig. 5, the maximum of the H_2-TPR profiles shifts from 205 to 230 °C due to the slight increase in the particle size, as was inferred from the

Table 3
Metallic properties of 10Cu-Y catalysts determined by N_2O titration.

Catalyst	Metallic surface area		Dispersion	Particle size
	m^2_{Cu} g_{Cu}^{-1}	m^2_{Cu} g_{cat}^{-1}	%	nm
10Cu-SBA-LT	238	23.8	37	2.8
10Cu-SBA-HT	210	21.0	32	3.2
10Cu-MFC-LT	259	25.9	39	2.6
10Cu-SiO_2	182	18.2	28	3.7

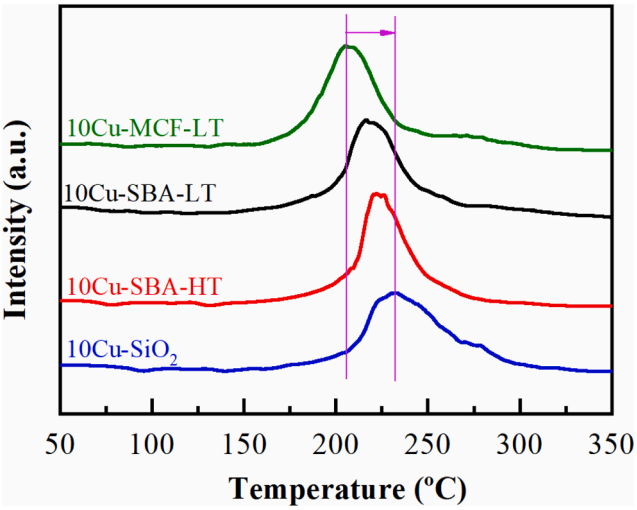

Fig. 5. H_2-TPR profiles of 10Cu-Y catalysts.

N_2O titration (Table 3). Thus, copper nanoparticles are more easily reduced in the case of 10Cu-MCF-LT than in 10Cu-SiO_2. With respect to the samples supported on SBA-15, the maximum slightly shifted toward a higher temperature for 10Cu-SBA-HT compared to 10Cu-SBA-LT, which could be attributed to those agglomerated particles detected by TEM (Fig. 4) that would be more difficult to reduce. Additionally, in most H_2-TPR profiles, and mainly in the case of 10Cu-SiO_2, a shoulder is observed at higher reduction temperatures, which could imply the existence of a small fraction of bigger Cu^{2+} nanoparticles that require even higher temperatures to be reduced.

In order to analyze the chemical composition on the surface, including the oxidation state of the active phase, XPS analyses were also carried out (Fig. 6 and Table 4). The Cu 2p core level spectra analysis for the Cu-based catalysts with a theoretical Cu loading of 10 wt% (Fig. 6A) shows a band located between 932.6 and 932.9 eV, which is ascribed to reduced Cu species [65]. However, as it is not possible to differentiate between Cu^+ and Cu^0 species, it is also necessary to use the Cu_{LMM} Auger line (Fig. 6B). The coexistence of Cu^0 and Cu^+ is observed in all cases, being Cu^+ the most abundant (56.6–60.2%) (Table 4). The presence of Cu^0 and Cu_2O agrees with XRD data (Fig. 3), although those showed more intense peaks for Cu^0 species. The higher proportion of Cu^+ species could be ascribed to partial oxidation of Cu^0 species during handling, or to the presence of small Cu_2O particles well dispersed on the surface, which would be hardly observed by XRD. On the other hand, in the Si 2p core level spectra, there is a contribution located at about 103.3–103.5 eV, which is typical of SiO_2 [65], while the O 1 s core level spectra also show the characteristic band of oxygen in SiO_2 at about 532.7–532.8 eV (Table 4) [65].

The surface Cu composition obtained by XPS analysis of the Cu-based catalysts with a 10 wt% theoretical Cu content is between 1.0 and 2.2% (Table 4). On those catalysts with greater dispersion and consequently smaller particle size, one should expect higher surface copper contents. However, this is not the case when comparing the dispersion obtained by N_2O titration (Table 3) and the XPS results (Table 4). In this sense, TEM micrographs have revealed that, in the case of 10Cu-SBA-LT (Fig. 4A) and especially on 10Cu-SBA-HT (Fig. 4B), there is a large proportion of Cu nanoparticles deposited on the external surface of the porous structures, whereas smaller particles are able to penetrate into the pores of 10Cu-MCF-LT (Fig. 4C2). Taking this premise into account and considering that XPS is a surface technique, it is possible to justify the higher surface Cu content on 10Cu-SBA-LT and 10Cu-SBA-HT when compared to 10Cu-MCF-LT.

The quantification of the acid sites, performed by NH_3-TPD (Table 1), reveals a relatively low concentration between 32 and 57 μmol g^{-1} for

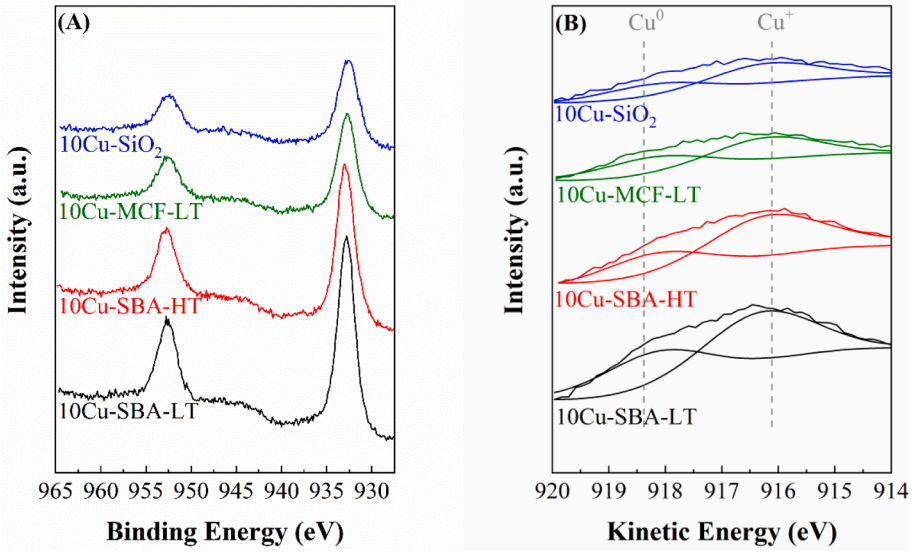

Fig. 6. Cu 2p core level spectra (A) and Cu_{LMM} Auger lines (B) for 10Cu-Y catalysts.

Table 4
Spectral parameters obtained for 10Cu-Y catalysts, as determined by XPS.

Catalyst	Binding Energy, eV (Atomic concentration, %)				Cu_{LMM} Auger (Atomic concentration, %)	
	C 1 s	O 1 s	Si 2p	Cu 2p	Cu^0	Cu^+
10Cu-SBA-LT	284.8 (12.2)	532.8 (58.8)	103.5 (28.4)	932.8 (1.5)	918.2 (41.8)	916.4 (58.2)
10Cu-SBA-HT	284.8 (8.2)	532.8 (60.2)	103.4 (29.3)	932.9 (2.2)	918.2 (42.2)	916.0 (57.8)
10Cu-MCF-LT	284.8 (6.1)	532.8 (63.5)	103.5 (29.2)	932.7 (1.2)	918.2 (43.4)	916.3 (56.6)
10Cu-SiO_2	284.8 (6.3)	532.7 (59.6)	103.3 (33.0)	932.6 (1.0)	918.2 (39.8)	916.3 (60.2)
10Cu-MCF-LT (48 h)	284.8 (39.5)	532.5 (42.3)	103.1 (17.6)	932.6 (0.4)	918.2 (40.0)	916.4 (60.0)

all the 10Cu-Y catalysts. This low acidity is mainly ascribed to the Brönsted acid sites associated to silanol groups that have not been involved in the SEA process, whereas the existence of Lewis acid sites can be assigned to Cu^+ species, which are more easily formed when small Cu^0 particles are present. The acidity is necessary to obtain MF, although the amount and strength of those acid sites need to be modulated to minimize the deactivation in the gas-phase hydrogenation of FUR. It should also be noted that 10Cu-MCF-LT showed the lowest acidity. Regarding the density of acid sites, 10Cu-SiO_2 exhibited the highest value, while 10Cu-MCF-LT showed the lowest one, despite having a surface area similar to that of 10Cu-SBA-LT and 10Cu-SBA-HT.

3.2. Catalytic results

These Cu-based catalysts with different textural properties were studied in the gas-phase FUR hydrogenation. In this work, the catalytic conditions were selected to observe the differences between the catalysts prepared with different silica supports, instead of choosing the best

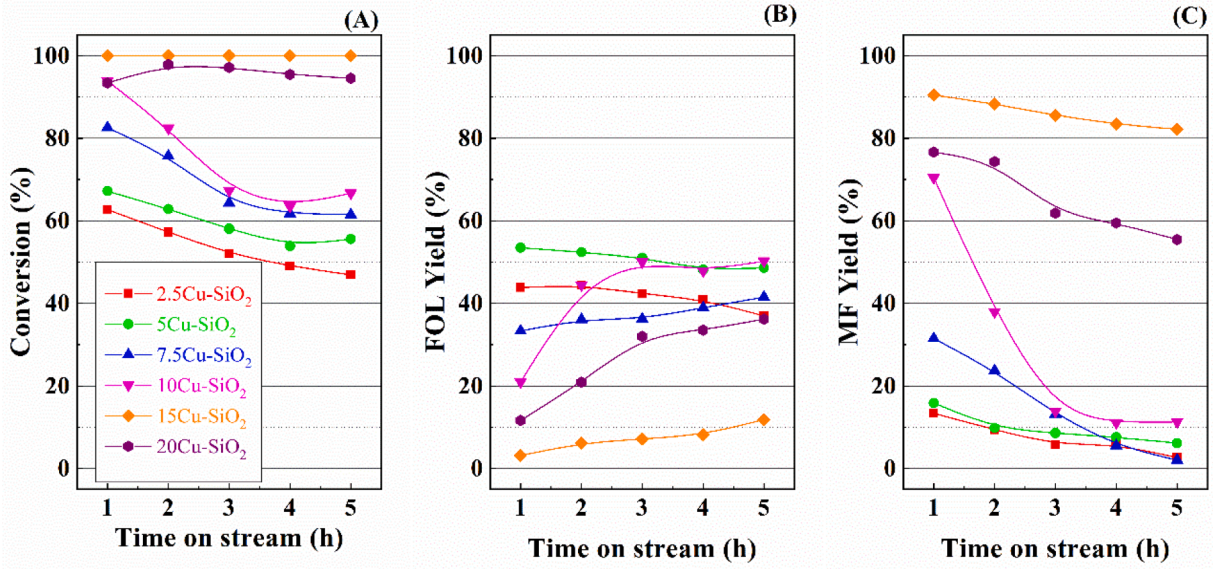

Fig. 7. FUR conversion (A), FOL yield (B), and MF yield (C) in the FUR hydrogenation over XCu-SiO_2 catalysts with a Cu loading between 2.5 and 20 wt%. Experimental conditions: mass of catalyst = 0.15 g, temperature = 190 °C, pressure = 0.1 MPa, H_2 flow = 10 mL min^{-1}, and feed flow = 2.3 $mmol_{FUR}$ h^{-1}.

experimental conditions to achieve the complete conversion of furfural. In addition, the physico-chemical characterization of fresh and used catalysts also allows to elucidate the causes of the observed deactivation of the catalysts.

The first study focused on the influence of the Cu loading on the catalytic behavior. For this purpose, the commercial SiO_2 with Cu contents between 2.5 and 20 wt% was selected (Fig. 7). In most cases, it was observed a progressive decrease in the FUR conversion with time-on-stream (TOS) (Fig. 7A), being more pronounced with those catalysts with Cu loadings lower than 15 wt%. Thus, FUR conversion increases from 47% for 2.5Cu-SiO_2 to almost full conversion for 15Cu-SiO_2 after 5 h of TOS at 190 °C. It is striking that the catalytic activity slightly decreased for the catalyst with the highest Cu content (20Cu-SiO_2) compared to 15Cu-SiO_2 under similar experimental conditions. In this sense, previous research studies have shown similar trends with other Cu/SiO_2 catalysts with small particle sizes [37]. In that study, it was observed that the increase in the Cu content caused the sintering of metal particles, thus decreasing the metallic surface area (i.e., amount of available active sites).

Regarding the product distribution (Fig. 7B-C), the catalysts with lower Cu contents tend to form a larger amount of FOL, even at short reaction times, with the 5Cu-SiO_2 catalyst reaching the highest FOL yield after 1 h of TOS at 190 °C (54%), with this slightly decreasing to 49% after 5 h of TOS. An increase in the Cu loading causes a progressive decrease in the FOL yield, which is accompanied by a rise in the MF yield. This trend is clearly observed in the case of 10Cu-SiO_2, although the MF yield decreases from 70% after 1 h to 12% after 5 h of TOS at 190 °C. On the contrary, the FOL yield increases from 19% after 1 h to 51% after 5 h of TOS at 190 °C.

Considering that all catalysts display similar acidity and metal particle size, these should show similar catalytic behavior. Thus, it is expected that all catalysts are highly selective towards MF at t_0; however, the hydrogenolysis sites (FOL → MF) in the catalysts with lower Cu content (lower metallic surface areas) are poisoned very fast, in such a way that FOL is the main product after the first hour of reaction. In the case of the catalysts with higher Cu contents, their higher metallic surface areas maintain the hydrogenolysis process along the TOS, reaching a MF yield of 82% with the 15Cu-SiO_2 catalyst after 5 h of TOS at 190 °C. In any case, the hydrogenolysis sites involved in the FOL → MF reaction are more susceptible to deactivate than the hydrogenation sites involved in FUR → FOL, as the increase in the FOL yield with TOS suggests. Interestingly, the 20Cu-SiO_2 catalyst provides a lower proportion of MF and larger FOL after 5 h of TOS compared with the product distribution at the beginning of the reaction. These data are in agreement with a previous study in which it was demonstrated that the incorporation of higher Cu loadings led to the formation of bigger Cu nanoparticles, which favor the hydrogenation reaction (FUR → FOL) with respect to the hydrogenolysis reaction (FOL → MF) [37]. In this sense, Shan et al. pointed out that the formation of Cu–O-Si-O- bonds favored the formation of Lewis acid sites, even under H_2 flow, which can be involved in the hydrogenolysis step [66]. In this regard, the presence of Cu^+ species, identified by XRD (Figs. 1 and 3), may also imply the existence of Lewis acid sites, which may be involved in the FOL → MF hydrogenolysis process [66,67].

The catalytic activity reported in Fig. 7A follows a similar trend to the metallic surface area ($m^2\ g_{cat}^{-1}$) shown in Table 2, in such a way that a higher content of available Cu sites provides a greater catalytic activity and resistance against deactivation. Consequently, the catalyst with the highest metallic surface area (15Cu-SiO_2) is the most active. However, the catalyst with the highest Cu content (20Cu-SiO_2) displays a selectivity pattern that resembles that of 7.5Cu-SiO_2 and 10Cu-SiO_2 catalysts, even though the catalytic activity almost stays unaltered, which is likely due to the decreased metallic surface area and the stronger deactivation of the hydrogenolysis sites (FOL → MF).

These results have been compared with those obtained with copper chromite, the commercial catalyst used in the industrial process, under similar experimental conditions [68]. It should be noted that copper chromite reached a FUR conversion of about 75% after 30 min of reaction, but it was very prone to deactivation, with negligible activity after 5 h of reaction. Regarding the selectivity, the main product was FOL with a selectivity above 90%. Those data differ from the reported in the present work because deactivation is more limited and the main product, especially at short reaction times, is MF, which indicates that the hydrogenolysis reaction FOL → MF is promoted due to the presence of a small fraction of weak acid sites.

Taking into account that 10Cu-SiO_2 is the most prone catalyst to modify its selectivity pattern with TOS (Fig. 7A) and that this catalyst does not maintain a total conversion, a 10 wt% loading was selected to study the influence of the textural properties and morphology of the porous silica on the catalytic behavior (Fig. 8). Considering that all catalysts display similar Cu crystallite size (Table 3) and active site-support interaction (Cu-SiO_2), the difference in the catalytic behavior must be ascribed to the textural properties of the catalysts.

The data reveal that all the catalysts, except 10Cu-SBA-HT, reach high conversion values at short TOS, with initial values close to 100% (Fig. 8A). While 10Cu-SBA-LT and 10Cu-MCF-LT render FUR conversions higher than 90% after 5 h of TOS at 190 °C, 10Cu-SiO_2 deactivates (FUR conversion of 66% after 5 h of TOS). However, in the case of 10Cu-SBA-HT, the conversion is low from the beginning of the reaction, and the conversion decreases further after 5 h of TOS, obtaining the poorest FUR conversion (11%).

The analysis of the product distribution (Fig. 8B-C) reveals that the most active catalysts (10Cu-MCF-LT, 10Cu-SBA-LT, and even 10Cu-SiO_2) show higher MF yields (greater than 70%) at shorter reactions times (1 h), whereas 10Cu-SBA-HT is more selective towards FOL. As the reaction time progresses, the selectivity towards MF decreases, although the most active catalyst (10Cu-MCF-LT) still maintains a MF yield of 76% after 5 h of TOS at 190 °C. The deactivation process is accompanied by a concomitant increase in the formation of FOL, obtaining the highest FOL yield of 49% with the 10Cu-SiO_2 catalyst after 5 h of TOS. Interestingly, the formation of FOL is more pronounced on the catalysts that deactivate. Therefore, it can be concluded that MF formation occurs through two consecutive reactions, FUR → FOL on hydrogenation sites, and FOL → MF on hydrogenolysis sites, which are more likely to be deactivated, as had previously been suggested by other authors [31,35,37]. In this respect, DFT studies have suggested that the first step, the hydrogenation reaction (FUR → FOL), occurs by the interaction of the Cu nanoparticles with the oxygen atom of the carbonyl group in a top η^1(O)-aldehyde binding mode [26]. In the second step, the hydrogenolysis reaction (FOL → MF), FOL adopts a similar disposition on the copper sites [31] through an interaction with the oxygen atom of the hydroxyl group, while the furan ring is nearly parallel to the surface. Several authors have pointed out that the existence of weak acidity, together with the presence of small Cu particles, favors the hydrogenolysis reaction [35,37]. However, the acidity cannot be high, as this would favor the polymerization and the strong adsorption of FUR on the catalyst surface, blocking the active sites in such a way that the catalysts suffer a drastic deactivation at short reaction times. NH_3-TPD data (Table 1) confirmed the low acidity of these catalysts; therefore, using the SEA method for the incorporation of small Cu nanoparticles onto amorphous and porous silica seems to be appropriate to minimize, or slow down, the generation of carbonaceous deposits. Considering that most of the catalysts here synthesized initially produce MF, it could be proposed that the acidity, even if low, would be associated with the silanol groups and partially reduced Cu species (Cu^+), which provide Lewis-type acidity. In fact, other authors concluded that small Cu^+ particles exhibited Lewis acidity, which promoted hydrogenolysis processes [66,67]. On the other hand, it should be noted that the hydrogenolysis reaction (FOL → MF) generates H_2O as a by-product, which might have an adverse effect on the catalytic performance as it could favor the oxidation of Cu^0 to Cu^+, thus increasing the Lewis acidity. In this sense, it has been reported in the literature that Cu^+ sites can

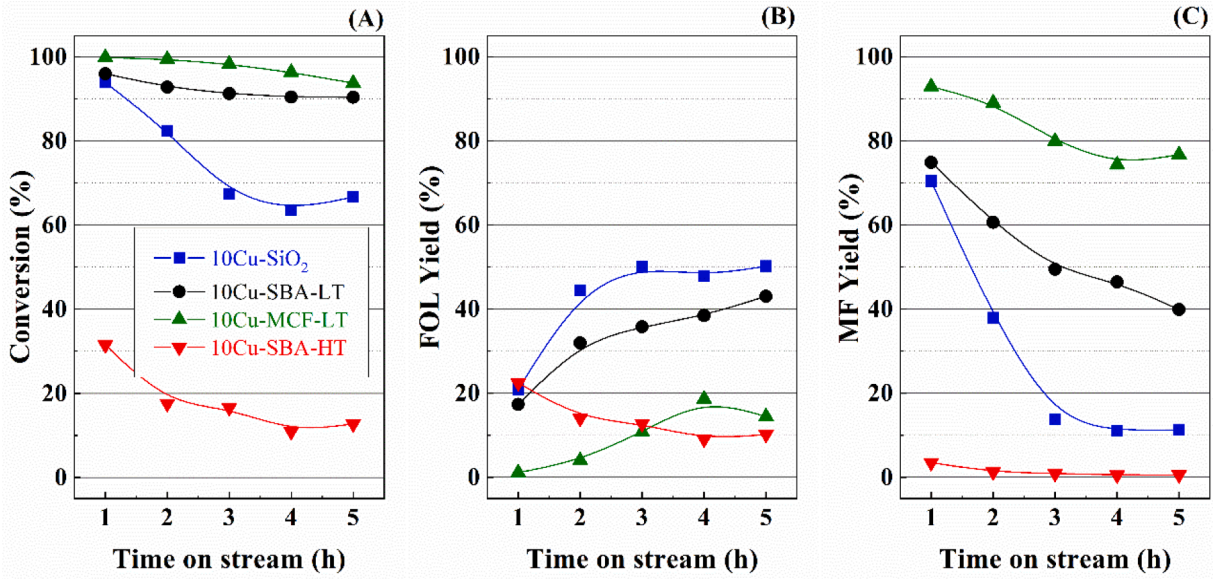

Fig. 8. FUR conversion (A), FOL yield (B), and MF yield (C) in the FUR hydrogenation over 10Cu-Y catalysts. Experimental conditions: mass of catalyst = 0.15 g, temperature = 190 °C, pressure = 0.1 MPa, H_2 flow = 10 mL min^{-1}, and feed flow = 2.3 $mmol_{FUR}$ h^{-1}.

interact more strongly with CO than the Cu^0 ones [69]. This fact can be extrapolated to the carbonyl group of the FUR molecule, being able to infer that the presence of a higher proportion of Cu^+ sites could favor a stronger interaction of the FUR molecules with the active centers, favoring a faster formation of carbonaceous deposits that block the active sites involved in the FUR hydrogenation. Moreover, previous studies have reported that the adsorption heats of FUR and H_2O are very similar (12.3 and 12.4 kcal mol^{-1}, respectively) [31,70]; therefore, they could compete for the same active centers, negatively affecting the catalytic behavior. In addition, the interaction of H_2O with FUR can also favor its polymerization. Thus, the presence of H_2O could promote the partial oxidation of copper species; however, the Cu^+/Cu^0 ratio detected by XPS was very similar in all cases, discarding its influence on the selectivity pattern. Taking into account all these premises, it seems clear that the sites involved in the second step (FOL → MF) are more prone to deactivate than those involved in the first step (FUR → FOL), as shown in Fig. 8B-C, since the decay of the formation of MF is accompanied by larger amounts of FOL. This fact could be explained by the formation of carbonaceous deposits that would mainly block those active sites involved in the hydrogenolysis reaction.

Considering that all the 10Cu-Y catalysts possess the same Cu loading (10 wt%) and all the supports have the same chemical composition (SiO_2), a similar catalytic behavior should be expected, although this is not the case (Fig. 8A). As previously stated, 10Cu-Y catalysts displayed different textural properties (Supplementary Information, Fig. S1 and Table 1), and those with the narrowest pore diameter between 3 and 7 nm (10Cu-MCF-LT and 10Cu-SBA-LT) provided the highest FUR conversions, likely due to the closer proximity of furfural to the active sites within the pores. Moreover, both catalysts exhibited the highest metallic surface area and, consequently, the lowest particle size (Table 3). Thus, a suitable pore size together with the small particle size could favor the reaction of FUR on the Cu sites. Conversely, the lower activity of the 10Cu-SBA-HT catalyst could be attributed to its pore diameter being too large (7–12 nm), which makes difficult the adsorption of FUR on the active sites, in such a way that FUR molecules can go across the SBA-15 mesochannels without interacting with the active sites. That catalyst also presents some agglomeration of the Cu nanoparticles on the outer surface, as observed by TEM (Fig. 4B). This was also observed by N_2O titration (Table 3), with 10Cu-SBA-HT and Cu-SiO_2 presenting the lowest dispersion values. On the other hand, when comparing the catalysts with narrower pore size distributions (10Cu-MCF-LT and 10Cu-SBA-LT), the 10Cu-SBA-LT catalyst is more prone to modify its selectivity pattern than 10Cu-MCF-LT. In this sense, even when the presence of narrow pores could favor the interaction between FUR and Cu sites, the longer channels could promote the subsequent interaction of FUR, or the reaction products, with the active centers, in such a way that these pores would be blocked. However, with the addition of fluoride in the synthesis step, the length of the silica channels decreases, which facilitates the furfural access and exit of the reaction products from the channels, thus showing a more gradual deactivation. On the other hand, the N_2O titration data also show that the 10Cu-MCF-LT catalyst displays the highest metallic surface area, so this catalyst possesses the highest number of available Cu sites for the FUR hydrogenation. It should also be noted that the density of acid sites on 10Cu-SBA-LT is twice that observed for 10Cu-MCF-LT, which could also contribute to a faster deactivation through the formation of carbonaceous deposits. Likewise, it was previously mentioned that the 10Cu-SiO_2 catalyst was more prone to deactivation, which agrees with its highest number of acid sites and the lowest metallic surface area. Therefore, it can be concluded that the 10Cu-MCF-LT catalyst possesses suitable textural and acidic properties to provide a high FUR conversion with a low deactivation rate.

The following study aims to evaluate the effect of the reaction temperature on the catalytic performance (Fig. 9). Considering that the boiling point of FUR is 161.7 °C, the catalytic studies were carried out between 170 and 230 °C. A volcano-type conversion as a function of temperature has been previously reported in the gas-phase hydrogenation of FUR [17,36,71]. Thus, the FUR conversion increases at lower reaction temperatures because the FUR hydrogenation is thermodynamically favored under those conditions [17]. However, higher temperatures worsen the catalytic performance due to the polymerization processes that take place, which cause a fast deactivation [17]. Furthermore, the hydrogenolysis reaction is favored at high temperatures [17,36]. As expected, the reaction at 170 °C provides the lowest conversion values (70% after 5 h of TOS), although the catalyst is highly selective to FOL (59% yield). Increasing the reaction temperature improves the FUR conversion, but it also modifies the selectivity pattern. Thus, at 190 °C, the FUR conversion is higher than 93% and the MF yield is above 75% in all cases, after 5 h of TOS, confirming that the hydrogenolysis reaction is favored at higher temperatures, as previously reported [36,71]. Surprisingly, a further increase of the reaction temperature did not decrease the conversion, as previously pointed out in the literature [17,36]. This could be due to the small size of the Cu

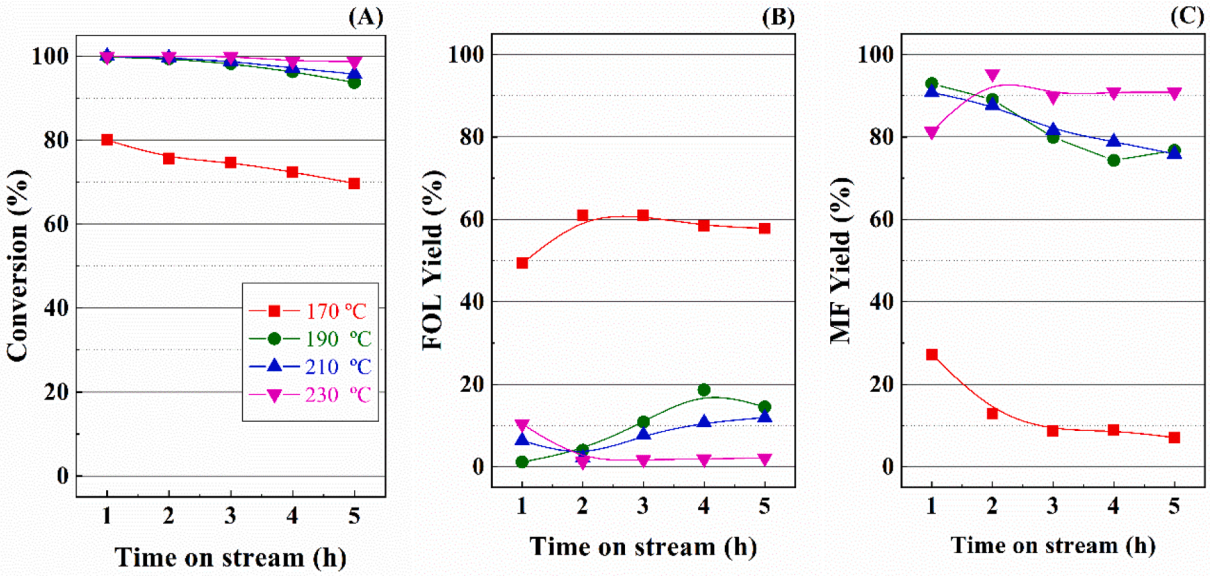

Fig. 9. FUR conversion (A), FOL yield (B), and MF yield (C) in the FUR hydrogenation over 10Cu-MCF-LT catalyst at different temperatures. Experimental conditions: mass of catalyst = 0.15 g, pressure = 0.1 MPa, H_2 flow = 10 mL min^{-1}, and feed flow = 2.3 $mmol_{FUR}$ h^{-1}.

crystallites (<4 nm), which implies that the metallic surface area is very high, so that the catalysts are more resistant to deactivation than others with bigger metal nanoparticles [36–38]. It has also been demonstrated that the 10Cu-MCF-LT catalyst possessed a lower density of acid sites and suitable textural properties due to the use of fluoride for the synthesis of this support, which could contribute to slowing down its deactivation.

Finally, in order to further evaluate the stability of the 10Cu-MCF-LT catalyst, another experiment was carried out at a longer reaction time (Fig. 10). This stability test was performed at 230 °C because high conversion and MF selectivity were observed under these experimental conditions, in order to determine if that high MF production could be maintained along with TOS. Even though 10Cu-MCF-LT showed almost complete conversion initially, it suffered gradual deactivation with TOS, obtaining a FUR conversion of 44% after 48 h of TOS. Regarding product distribution, the main product during the first hours of TOS is MF, resulting from the consecutive hydrogenation-hydrogenolysis reactions taking place. However, after 6 h of TOS, the MF selectivity decreases likely due to some metal sites involved in the hydrogenolysis reaction being blocked by carbonaceous deposits, as was previously reported [37], so that the FUR → FOL → MF process mostly ends in FOL, maintaining a FOL yield of 39% after 48 h. This fact confirms that the hydrogenation sites are less susceptible to deactivation than the hydrogenolysis ones. As the gas-phase FUR hydrogenation is a reaction that undergoes strong deactivation processes, it is essential to evaluate the regeneration capacity of catalysts. According to previous studies, the carbonaceous deposits involved in the deactivation could be removed by calcination at 500 °C [36,37]. After calcination at this temperature, 10Cu-MCF-LT displayed a lower FUR conversion value (80%) than the first cycle (Fig. 10). However, the deactivation follows the same trend to

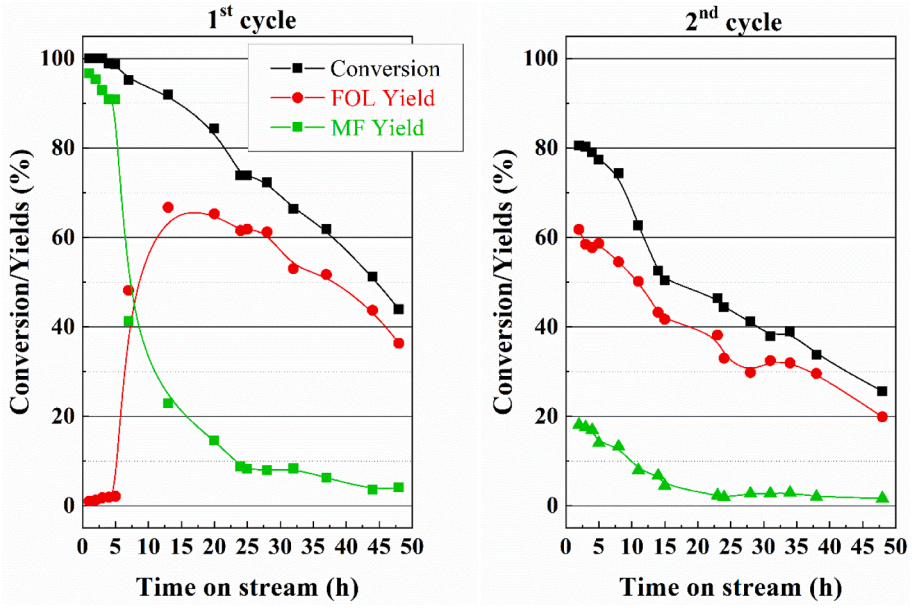

Fig. 10. FUR conversion, FOL yield, and MF yield in the FUR hydrogenation over the 10Cu-MCF-LT catalyst: 1st cycle (A) and 2nd cycle (B) (with regeneration by calcination at 500 °C). Experimental conditions: mass of catalyst = 0.15 g, temperature = 230 °C, pressure = 0.1 MPa, H_2 flow = 10 mL min^{-1}, and feed flow = 2.3 $mmol_{FUR}$ h^{-1}.

that observed along the first run, obtaining a conversion of 25% after 48 h of TOS. Nevertheless, the selectivity profile is different to that shown after the first run, with FOL as the main product (62% FOL yield after 1 h) instead of MF. The change in the selectivity pattern is ascribed to an increase in the Cu particle size during the regeneration process, which is reflected on the loss of the hydrogenolysis sites due to the reduction of the metallic surface area. In this sense, it has been reported in the literature that Cu-based catalyst favor the formation of MF in gas-phase when Cu nanoparticles sizes are lower than 5 nm [35,37,64], due to the generation of Lewis acid sites [72] besides those associated to the slightly acidic silica support [35,37].

In order to elucidate the changes of the active phase throughout the catalytic tests, the 10Cu-MFC-RT catalyst was collected after two cycles of 48 h of TOS at 230 °C. XRD analysis shows that the 10Cu-MFC-RT catalyst hardly suffered any changes (Fig. S2), discarding the transformation of Cu_2O, or Cu^0, in other crystalline phases. However, the XPS analysis revealed that the proportion of Cu^+ remained almost unchanged after two cycles of 48 h (Fig. S3). While the presence of Cu^+ species could favor the hydrogenolysis reaction to produce MF, the modification of the selectivity pattern would indicate that the presence of Cu^+ does not have a predominant role in determining the selectivity pattern, as inferred from a higher production of FOL.

From the XPS data (Fig. S3 and Table 4), it is observed a decrease in the intensity of the Cu 2p core level spectrum and the Cu $Auger_{LMM}$ line after the two catalytic cycles, which suggests a decrease in the dispersion of Cu species on the catalyst surface. The analysis of the surface chemical composition, before and after the catalytic cycles, also shows an increase in the carbon content after the reaction (Table 4), confirming that a fraction of the Cu species could be partially blocked by the formation of carbonaceous deposits (polymerized FUR and FOL), which seems to agree with the progressive decline of the FUR conversion.

4. Conclusions

A series of Cu-based catalysts was prepared by the strong electrostatic adsorption (SEA) method using several silica supports with different morphologies and textural properties (commercial fumed silica, SBA-15 synthesized at room temperature and under hydrothermal conditions, and mesocellular foam), and these were studied in the gas-phase hydrogenation of furfural, obtaining Cu^0 crystallites with a size below 5 nm. Regarding Cu supported on mesoporous silica catalysts, it can be concluded that the presence of large pores (greater than 7 nm), like those found on the SBA-15 synthesized under hydrothermal conditions, complicated the intimate interaction between the reagents and the active sites along the channels, giving rise to very low catalytic activity. In addition, this catalyst also showed that the agglomeration of the Cu nanoparticles could worsen the activity even more. In contrast, mesoporous silica supports synthesized at room temperature, 10Cu-SBA-LT and 10Cu-MCF-LT catalysts, offered a more suitable pore size for reaction. Moreover, it was demonstrated that the addition of fluoride on the synthesis shortened the length of the silica channels (mesocellular foam), which facilitates the furfural access and exit of the reaction products on 10Cu-MCF-LT, thus providing the highest values of furfural conversion and 2-methylfuran yield. Besides, the high production of 2-methylfuran at the beginning of the reaction could be attributed to the low acidity of this catalyst. However, its selectivity pattern changed along 48 h of TOS, even after intermediate catalyst regeneration, due to the fact that hydrogenolysis sites are more prone to deactivation processes.

Declaration of Competing Interest

The authors declare that they have no known competing financial interests or personal relationships that could have appeared to influence the work reported in this paper.

Acknowledgments

The authors are grateful for financial support from the Spanish Ministry of Science, Innovation and Universities (RTI2018-94918-B-C44 project), FEDER (European Union) funds (UMA18-FEDERJA-171 and UMA20-FEDERJA-88), Junta de Andalucía (P20-00375), and the University of Malaga. C.P.J.G. and C.G.S. acknowledge Junta de Andalucía and FEDER funds, respectively, for their postdoctoral contracts. A.C.A.R. is thankful to the University of Toledo for her start-up package. Funding for open access charge was provided by the University of Malaga/CBUA.

Appendix A. Supplementary data

Supplementary data to this article can be found online at https://doi.org/10.1016/j.fuel.2022.123827.

References

[1] George WH, Sara I, Avelino C. Synthesis of transportation fuels from biomass: chemistry, catalysts, and engineering. Chem Rev 2006;2:4044–98. https://doi.org/10.1021/cr068360d.
[2] Chiang KY, Chien KL, Lu CH. Characterization and comparison of biomass produced from various sources: Suggestions for selection of pretreatment technologies in biomass-to-energy. Appl Energy 2012;100:164–71. https://doi.org/10.1016/j.apenergy.2012.06.063.
[3] Liu Y, Nie Yi, Lu X, Zhang X, He H, Pan F, et al. Cascade utilization of lignocellulosic biomass to high-value products. Green Chem 2019;21(13):3499–535.
[4] Chen H. Chemical composition and structure of natural lignocellulose. In: Chen H, editor. Biotechnology of Lignocellulose. Dordrecht: Springer Netherlands; 2014. p. 25–71.
[5] Wang S, Ru B, Dai G, Sun W, Qiu K, Zhou J. Pyrolysis mechanism study of minimally damaged hemicellulose polymers isolated from agricultural waste straw samples. Bioresour Technol 2015;190:211–8. https://doi.org/10.1016/j.biortech.2015.04.098.
[6] Mamman AS, Lee J-M, Kim Y-C, Hwang IT, Park N-J, Hwang YK, et al. Furfural: hemicellulose/xylose-derived biochemical. Biofuels, Bioprod Biorefining 2008;2(5):438–54.
[7] Choudhary V, Pinar AB, Sandler SI, Vlachos DG, Lobo RF. Xylose isomerization to xylulose and its dehydration to furfural in aqueous media. ACS Catal 2011;1:1724–8. https://doi.org/10.1021/cs200461t.
[8] Werpy T, Petersen G. Top value added chemicals from biomass volume I. US Dep Energy 2004;1:76. https://doi.org/10.2172/15008859.
[9] Yebo D. Furfural market. DalinYebo Trading and Development (Pty) Limited. http://www.dalinyebo.com/furfural-market 2014.
[10] Zeitsch KJ. The chemistry and technology of furfural and its many by-products. Amsterdam: Elsevier; 2000.
[11] Mariscal R, Maireles-Torres P, Ojeda M, Sádaba I, López GM. Furfural: a renewable and versatile platform molecule for the synthesis of chemicals and fuels. Energy Environ Sci 2016;9:1144–89. https://doi.org/10.1039/c5ee02666k.
[12] Yan K, Wu G, Lafleur T, Jarvis C. Production, properties and catalytic hydrogenation of furfural to fuel additives and value-added chemicals. Renew Sustain Energy Rev 2014;38:663–76. https://doi.org/10.1016/j.rser.2014.07.003.
[13] Adkins H, Connor R. The catalytic hydrogenation of organic compounds over copper chromite. J Am Chem Soc 1931;53:1091–5. https://doi.org/10.1021/ja01354a041.
[14] Calingaert G, Edgar G. Small-plant-scale liquid-phase hydrogenation under high pressure: hydrogenation of furfural. Ind Eng Chem 1934;26:878–80. https://doi.org/10.1021/ie50296a017.
[15] Brown HD, Hixon RM. Vapor phase hydrogenation of FurFural to FurFuryl alcohol. Ind Eng Chem 1949;41:1382–5. https://doi.org/10.1021/ie50475a021.
[16] Manly DG, Catalytic DAP, Hydrogenation I. Kinetics and catalyst composition in the preparation of 2-methylfuran. J Org Chem 1958;23:1093–5. https://doi.org/10.1021/jo01102a002.
[17] Liu D, Zemlyanov D, Wu T, Lobo-Lapidus RJ, Dumesic JA, Miller JT, et al. Deactivation mechanistic studies of copper chromite catalyst for selective hydrogenation of 2-furfuraldehyde. J Catal 2013;299:336–45.
[18] Ghashghaee M, Shirvani S, Ghambarian M. Kinetic models for hydroconversion of furfural over the ecofriendly Cu-MgO catalyst: an experimental and theoretical study. Appl Catal A Gen 2017;545:134–47. https://doi.org/10.1016/j.apcata.2017.07.040.
[19] Tukacs JM, Bohus M, Dibó G, Mika LT. Ruthenium-catalyzed solvent-free conversion of furfural to furfuryl alcohol. RSC Adv 2017;7:3331–5. https://doi.org/10.1039/c6ra24723g.
[20] Jiménez-Gómez CP, Cecilia JA, Moreno-Tost R, Maireles-Torres P. Selective furfural hydrogenation to furfuryl alcohol using Cu-based catalysts supported on clay minerals. Top Catal 2017;60:1040–53. https://doi.org/10.1007/s11244-017-0804-2.
[21] Shirvani S, Ghashghaee M, Farzaneh V, Sadjadi S. Influence of catalyst additives on vapor-phase hydrogenation of furfural to furfuryl alcohol on impregnated copper/

magnesia. Biomass Convers Biorefinery 2018;8:79–86. https://doi.org/10.1007/s13399-017-0244-z.
[22] Sadjadi S, Farzaneh V, Shirvani S, Ghashghaee M. Preparation of Cu-MgO catalysts with different copper precursors and precipitating agents for the vapor-phase hydrogenation of furfural. Korean J Chem Eng 2017;34:692–700. https://doi.org/10.1007/s11814-016-0344-7.
[23] Guo H, Zhang H, Zhang L, Wang C, Peng F, Huang Q, et al. Selective hydrogenation of furfural to furfuryl alcohol over acid-activated attapulgite-supported NiCoB amorphous alloy catalyst. Ind Eng Chem Res 2018;57(2):498–511.
[24] Guo H, Zhang H, Tang W, Wang C, Huang C, Chen P, et al. Furfural hydrogenation over amorphous alloy catalysts prepared by different reducing agents. BioResources 2017;12(4):8755–74.
[25] Ghashghaee M, Shirvani S, Farzaneh V, Sadjadi S. Hydrotalcite-impregnated copper and chromium-doped copper as novel and efficient catalysts for vapor-phase hydrogenation of furfural: effect of clay pretreatment. Braz J Chem Eng 2018;35:669–78. https://doi.org/10.1590/0104-6632.20180352s20160703.
[26] Sitthisa S, Resasco DE. Hydrodeoxygenation of furfural over supported metal catalysts: a comparative study of Cu, Pd and Ni. Catal Lett 2011;141:784–91. https://doi.org/10.1007/s10562-011-0581-7.
[27] Jiménez-Gómez CP, Cecilia JA, García-Sancho C, Moreno-Tost R, Maireles-Torres P. Selective production of furan from gas-phase furfural decarbonylation on Ni-MgO catalysts. ACS Sustain Chem Eng 2019;7:7676–85. https://doi.org/10.1021/acssuschemeng.8b06155.
[28] Guerrero-Torres A, Jiménez-Gómez CP, Cecilia JA, García-Sancho C, Franco F, Quirante-Sánchez JJ, et al. Ni supported on sepiolite catalysts for the hydrogenation of furfural to value-added chemicals: influence of the synthesis method on the catalytic performance. Top Catal 2019;62(5-6):535–50.
[29] Sulmonetti TP, Pang SH, Claure MT, Lee S, Cullen DA, Agrawal PK, et al. Vapor phase hydrogenation of furfural over nickel mixed metal oxide catalysts derived from layered double hydroxides. Appl Catal A Gen 2016;517:187–95.
[30] Manikandan M, Venugopal AK, Prabu K, Jha RK, Thirumalaiswamy R. Role of surface synergistic effect on the performance of Ni-based hydrotalcite catalyst for highly efficient hydrogenation of furfural. J Mol Catal A Chem 2016;417:153–62. https://doi.org/10.1016/j.molcata.2016.03.019.
[31] Shi Y, Zhu Y, Yang Y, Li Y-W-Y-W, Jiao H. Exploring furfural catalytic conversion on Cu(111) from computation. ACS Catal 2015;5:4020–32. https://doi.org/10.1021/acscatal.5b00303.
[32] O'Driscoll Á, Leahy JJ, Curtin T. The influence of metal selection on catalyst activity for the liquid phase hydrogenation of furfural to furfuryl alcohol. Catal Today 2017;279:194–201.
[33] Wang Y, Zhao D, Rodríguez-Padrón D, Len C. Recent advances in catalytic hydrogenation of furfural. Catalysts 2019;9:796. https://doi.org/10.3390/catal9100796.
[34] Sitthisa S, Sooknoi T, Ma YG, Balbuena PB, Resasco DE. Kinetics and mechanism of hydrogenation of furfural on Cu/SiO_2 catalysts. J Catal 2011;277:1–13. https://doi.org/10.1016/j.jcat.2010.10.005.
[35] Dong F, Zhu YY, Zheng H, Zhu YY, Li X, Li Y. Cr-free Cu-catalysts for the selective hydrogenation of biomass-derived furfural to 2-methylfuran: the synergistic effect of metal and acid sites. J Mol Catal A Chem 2015;398:140–8. https://doi.org/10.1016/j.molcata.2014.12.001.
[36] Jiménez-Gómez CP, Cecilia JA, Durán-Martín D, Moreno-Tost R, Santamaría-González J, Mérida-Robles J, et al. Gas-phase hydrogenation of furfural to furfuryl alcohol over Cu/ZnO catalysts. J Catal 2016;336:107–15.
[37] Jiménez-Gómez CP, Cecilia JA, Moreno-Tost R, Maireles-Torres P. Selective production of 2-methylfuran by gas-phase hydrogenation of furfural on copper incorporated by complexation in mesoporous silica catalysts. ChemSusChem 2017;10:1448–59. https://doi.org/10.1002/cssc.201700086.
[38] Bertolini GR, Jiménez-Gómez CP, Cecilia JA, Maireles-Torres P. Gas-phase hydrogenation of furfural to furfuryl alcohol over Cu-ZnO-Al_2O_3 catalysts prepared from layered double hydroxides. Catalysts 2020;10:486. https://doi.org/10.1201/9780429022944-22.
[39] Jiao L, Regalbuto JR. The synthesis of highly dispersed noble and base metals on silica via strong electrostatic adsorption: I. Amorphous silica. J Catal 2008;260:329–41. https://doi.org/10.1016/j.jcat.2008.09.022.
[40] Wong A, Liu Q, Griffin S, Nicholls A, Regalbuto JR. Synthesis of ultrasmall, homogeneously alloyed, bimetallic nanoparticles on silica supports. Science (80-) 2017;358:1427–30. https://doi.org/10.1126/science.aao6538.
[41] Kresge CT, Leonowicz ME, Roth WJ, Vartuli JC, Beck JC. Ordered mesoporous molecular sieves synthesized by a liquid-crystal template mechanism. Nature 1992;359:710–3. https://doi.org/10.1038/359710a0.
[42] Cecilia JA, Tost RM, Millán MR. Mesoporous materials: from synthesis to applications. Int J Mol Sci 2019;20:3213. https://doi.org/10.3390/ijms20133213.
[43] Zhao D, Feng J, Huo Q, Melosh N, Fredrickson GH, Chmelka BF, et al. Triblock copolymer syntheses of mesoporous silica with periodic 50 to 300 angstrom pores. Science (80-) 1998;279(5350):548–52.
[44] Argyle MD, Bartholomew CH. Heterogeneous catalyst deactivation and regeneration: a review. Catalysts 2015;5:145–269. https://doi.org/10.3390/catal5010145.
[45] Vilarrasa-Garcia E, Moya EMO, Cecilia JA, Cavalcante CL, Jiménez-Jiménez J, Azevedo DCS, et al. CO_2 adsorption on amine modified mesoporous silicas: Effect of the progressive disorder of the honeycomb arrangement. Microporous Mesoporous Mater 2015;209:172–83.
[46] Cecilia JA, Vilarrasa-García E, Morales-Ospino R, Bastos-Neto M, Azevedo DCS, Rodríguez-Castellón E. Insights into CO_2 adsorption in amino-functionalized SBA-15 synthesized at different aging temperature. Adsorption 2020;26:225–40. https://doi.org/10.1007/s10450-019-00118-1.
[47] Jana SK, Nishida R, Shindo K, Kugita T, Namba S. Pore size control of mesoporous molecular sieves using different organic auxiliary chemicals. Microporous Mesoporous Mater 2004;68:133–42. https://doi.org/10.1016/j.micromeso.2003.12.010.
[48] Vilarrasa-García E, Cecilia JA, Santos SML, Cavalcante CL, Jiménez-Jiménez J, Azevedo DCS, et al. CO_2 adsorption on APTES functionalized mesocellular foams obtained from mesoporous silicas. Microporous Mesoporous Mater 2014;187:125–34.
[49] Sayari A, Kruk M, Jaroniec M, Moudrakovski IL. New approaches to pore size engineering of mesoporous silicates. Adv Mater 1998;10:1376–9. https://doi.org/10.1002/(SICI)1521-4095(199811)10:16<1376::AID-ADMA1376>3.0.CO;2-B.
[50] Lettow JS, Han YJ, Schmidt-Winkel P, Yang P, Zhao D, Stucky GD, et al. Hexagonal to mesocellular foam phase transition in polymer-templated mesoporous silicas. Langmuir 2000;16(22):8291–5.
[51] Fulvio PF, Pikus S, Jaroniec M. Tailoring properties of SBA-15 materials by controlling conditions of hydrothermal synthesis. J Mater Chem 2005;15:5049–53. https://doi.org/10.1039/B511346F.
[52] Santos SML, Cecilia JA, Vilarrasa-García E, Silva Junior IJ, Rodríguez-Castellón E, Azevedo DCS. The effect of structure modifying agents in the SBA-15 for its application in the biomolecules adsorption. Microporous Mesoporous Mater 2016;232:53–64. https://doi.org/10.1016/j.micromeso.2016.06.004.
[53] Williamson GK, Hall WH. X-ray line broadening line from filed aluminium and wolfram. Acta Metall 1953;1:22–31. https://doi.org/10.1016/0001-6160(53)90006-6.
[54] Brunauer S, Emmett PH, Teller E. Adsorption of gases in multimolecular layers. J Am Chem Soc 1938;60:309–19. https://doi.org/10.1021/ja01269a023.
[55] de Boer JH, Lippens BC, Linsen BG, Broekhoff JCP, van den Heuvel A, Osinga TJ. Thet-curve of multimolecular N2-adsorption. J Colloid Interface Sci 1966;21:405–14. https://doi.org/10.1016/0095-8522(66)90006-7.
[56] Barrett EP, Joyner LG, Halenda PP. The determination of pore volume and area distributions in porous substances. J Am Chem Soc 1951;73:373–80. https://doi.org/https://doi.org/10.1021/ja01145a126.
[57] Landers J, Gor GY, Neimark AV. Density functional theory methods for characterization of porous materials. Colloids Surfaces A Physicochem Eng Asp 2013;437:3–32. https://doi.org/10.1016/j.colsurfa.2013.01.007.
[58] Pakharukova VP, Moroz EM, Zyuzin DA, Ishchenko AV, Dolgikh LY, Strizhak PE. Structure of copper oxide species supported on monoclinic zirconia. J Phys Chem C 2015;119:28828–35. https://doi.org/10.1021/acs.jpcc.5b06331.
[59] Bergeret G, Gallezot. P. Particle Size and Dispersion Measurements. In Handbook of Heterogeneous Catalysis. Wiley-VCH. KGaA: Weinheim, Germany: 2008.
[60] Jiménez-Gómez CP, Cecilia JA, García-Sancho C, Moreno-Tost R, Maireles-Torres P. Gas phase hydrogenation of furfural to obtain valuable products using commercial Cr-free catalysts as an environmentally sustainable alternative to copper chromite. J Environ Chem Eng 2021;9:105468. https://doi.org/10.1016/j.jece.2021.105468.
[61] Thommes M, Kaneko K, Neimark A V., Olivier JP, Rodriguez-Reinoso F, Rouquerol J, et al. Physisorption of gases, with special reference to the evaluation of surface area and pore size distribution (IUPAC Technical Report). Pure Appl Chem 2015;87:1051–69. https://doi.org/10.1515/pac-2014-1117.
[62] Galarneau A, Cambon H, Di Renzo F, Fajula F. True microporosity and surface area of mesoporous SBA-15 silicas as a function of synthesis temperature. Langmuir 2001;17:8328–35. https://doi.org/10.1021/la0105477.
[63] Dong X, Ma X, Xu H, Ge Q. Comparative study of silica-supported copper catalysts prepared by different methods: formation and transition of copper phyllosilicate. Catal Sci Technol 2016;6:4151–8. https://doi.org/10.1039/c5cy01965f.
[64] Du H, Ma X, Yan P, Jiang M, Zhao Z, Zhang ZC. Catalytic furfural hydrogenation to furfuryl alcohol over Cu/SiO_2 catalysts: a comparative study of the preparation methods. Fuel Process Technol 2019;193:221–31. https://doi.org/10.1016/j.fuproc.2019.05.003.
[65] C.D. Wagner, J.F. Moulder, L.E. Davis WMR. Handbook of X-Ray Photoelectron Spectroscopy. 1992.
[66] Shan J, Liu H, Lu K, Zhu S, Li J, Wang J, et al. Identification of the dehydration active sites in glycerol hydrogenolysis to 1,2-propanediol over Cu/SiO_2 catalysts. J Catal 2020;383:13–23.
[67] Mazarío J, Concepción P, Ventura M, Domine ME. Continuous catalytic process for the selective dehydration of glycerol over Cu-based mixed oxide. J Catal 2020;385:160–75. https://doi.org/10.1016/j.jcat.2020.03.010.
[68] Vargas-Hernández D, Rubio-Caballero JM, Santamaría-González J, Moreno-Tost R, Mérida-Robles JM, Pérez-Cruz MA, et al. Furfuryl alcohol from furfural hydrogenation over copper supported on SBA-15 silica catalysts. J Mol Catal A Chem 2014;383-384:106–13.
[69] Cox DF, Schulz KH. Interaction of CO with Cu^+ cations: CO adsorption on Cu_2O (100). Surf Sci 1991;249:138–48. https://doi.org/10.1016/0039-6028(91)90839-K.
[70] Rioux RM, Vannice MA. Hydrogenation/dehydrogenation reactions: Isopropanol dehydrogenation over copper catalysts. J Catal 2003;216:362–76. https://doi.org/10.1016/S0021-9517(02)00035-0.
[71] Nagaraja BM, Siva Kumar V, Shasikala V, Padmasri AH, Sreedhar B, David Raju B, et al. A highly efficient Cu/MgO catalyst for vapour phase hydrogenation of furfural to furfuryl alcohol. Catal Commun 2003;4:287–93. https://doi.org/doi:10.1016/S1566-7367(03)00060-8.
[72] Scotti N, Dangate M, Gervasini A, Evangelisti C, Ravasio N, Zaccheria F. Unraveling the role of low coordination sites in a cu metal nanoparticle: a step toward the selective synthesis of second generation biofuels. ACS Catal 2014;4:2818–26. https://doi.org/10.1021/cs500581a.